An in situ synchrotron XAS methodology for surface analysis under high temperature, pressure, and shear

A. Dorgham, A. Neville, K. Ignatyev, F. Mosselmans, and A. Morina

Citation: Rev. Sci. Instrum. **88**, 015101 (2017); doi: 10.1063/1.4973354
View online: http://dx.doi.org/10.1063/1.4973354
View Table of Contents: http://aip.scitation.org/toc/rsi/88/1
Published by the American Institute of Physics

An *in situ* synchrotron XAS methodology for surface analysis under high temperature, pressure, and shear

A. Dorgham,[1,a)] A. Neville,[1] K. Ignatyev,[2] F. Mosselmans,[2] and A. Morina[1]
[1]*Institute of Functional Surfaces, School of Mechanical Engineering, University of Leeds, Leeds LS2 9JT, United Kingdom*
[2]*Diamond Light Source Ltd., Diamond House, Harwell Science and Innovation Campus, Didcot, Oxfordshire OX11 0DE, United Kingdom*

(Received 24 July 2016; accepted 14 December 2016; published online 3 January 2017)

The complex tribochemical nature of lubricated tribological contacts is inaccessible in real time without altering their initial state. To overcome this issue, a new design of a pin-on-disc tribological apparatus was developed and combined with synchrotron X-ray absorption spectroscopy (XAS). Using the designed apparatus, it is possible to study *in situ* the transient decomposition reactions of various oil additives on different surfaces under a wide range of realistic operating conditions of contact pressure (1.0–3.0 GPa), temperature (25–120 °C), and sliding speed (30–3000 rpm or 0.15–15 m/s). To test the apparatus, several tribological tests were performed at different shearing times ranging from 2.5 to 60 min. These tests were carried out under helium atmosphere at a temperature of 80 °C, contact pressure of 2.2 GPa, and sliding speed of 50 rpm. The XAS experiments indicate that the zinc dialkyldithiophosphate antiwear additive decomposes in the oil to form a tribofilm on the iron surface at different reaction kinetics from the ones of the thermal film. The tribofilm composition evolves much faster than the one of the thermal film, which confirms that the formation of the tribofilm is a thermally activated process similar to the one of the thermal film but accelerated by shear. Furthermore, the results indicate that the sulfur of the formed film, whether a tribofilm or a thermal film, appears initially in the form of sulfate, with some sulfide, which under heat or shear is reduced into mainly sulfide. *Published by AIP Publishing.* [http://dx.doi.org/10.1063/1.4973354]

I. INTRODUCTION

One of the biggest challenges for industry is friction and wear, which consume material, energy, and ultimately money. For example, in the automotive industry about 28% of the fuel energy is wasted due to friction losses in engine and transmission.[1] Therefore, by reducing friction by 1%, the annual fuel consumption worldwide is projected to be reduced by 1×10^9 l based on the total consumption in 2015.[2] Furthermore, more than 1.0% saving in the Gross National Product (GNP) of many industrial counties, such as the USA,[3] UK,[4] and China,[5] can be achieved through a proactive practice of tribology that optimizes friction, wear, and lubrication. One of the proactive measures taken by industry to reduce friction and wear is the use of oil additives such as molybdenum dithiocarbamate (MoDTC) and zinc dialkyldithiophosphate (ZDDP). MoDTC additive is used mainly as a friction modifier. It decomposes at high temperature and under shear to form MoS_2 sheets on the contacting surfaces, which reduce friction due to their interlayer sliding.[6] On the other hand, phosphorous containing additives such as ZDDP are widely used in the automotive industry as antiwear and antioxidant additives.[7] They can mitigate wear by forming a protective film, called tribofilm, on the contacting surfaces[8] and by breaking the surface oxidation cycle by decomposing peroxides and peroxy-radicals in the oil.[9]

Extensive experimental and modeling works have been carried out in order to understand the decomposition reactions of oil additives, the formation and removal of their formed tribofilms, and the possible synergy between them.[7,10] Nonetheless, the complete nature of the tribochemical reactions occurring on the surfaces under shear is still not fully understood. The rate of the decomposition reactions of oil additives and the associated rate of their tribofilms formation under different operating conditions and on different surfaces are still yet unexplored areas though highly important for optimizing the running-in period. Furthermore, the role of the available cations in the oil such as iron in the tribofilm formation is still controversial. Several studies[9,11–13] suggested that iron is needed for the formation of tribofilms such as the ones of ZDDPs. On the other hand, other studies[14–17] found that these tribofilms can form on surfaces other than iron.

The major obstacle in obtaining better understanding of the transient tribochemical nature at the tribological contacts is mainly due to the inability to probe the contact area directly. Most of the previous studies were carried out *ex situ* after the tribological test is stopped and the contacting surfaces are cooled down and separated. This alteration of the initial state of the sample brings about several limitations. First, the surface analysis will be performed under different conditions from the test environment. This can change the composition of the newly formed surface film by exposing it to a new environment of different temperature and relative humidity.[9,18] Furthermore, it can expose the surface to adventitious entities or contaminants such as carbon,[19] which can attenuate the measured atomic concentrations depending on the electrons

a)Author to whom correspondence should be addressed. Electronic mail: a.dorgham@leeds.ac.uk

inelastic mean free path through the elements under study.[20] Second, rinsing the surface with a solvent to remove the excess oil, which is the typical practice before carrying out the *ex situ* analysis especially under ultra-high vacuum (UHV) conditions, can remove part of the tribofilm layers and hence part of the information can be lost after washing.[21] Third, the fact that the surface can only be probed after finishing the tribological test prevents capturing the early stage of the tribofilm formation. Therefore, it can severely limit our understanding of the dynamical tribochemical nature of oil additives and it conceals the occurrence of any side reaction and the identification of any precursor or intermediate. Nonetheless, regardless of these limitations, several *ex situ* and *in situ* studies examined the tribological contacts after different shearing times and operating conditions, which provided significant insights into the complex tribochemistry of the additives decomposition and the formation of functional tribofilms.

The *ex situ* studies were carried out mainly using X-ray photoelectron spectroscopy (XPS),[19,22] Raman spectroscopy,[23,24] Fourier transform infrared (FT-IR) spectroscopy,[25] and X-ray absorption spectroscopy (XAS).[26,27] The XAS studies investigated the reactions of different oil additives including ZDDP,[14,28,29] ashless alkyldithiophosphate (DDP),[28,30] potassium triborate,[31] phosphate ester additives,[32] and other different organosulfur additives.[33] These studies examined the composition of the formed tribofilms, whether on iron,[34] Al–Si alloys,[14,35] or other coated surfaces.[34] In addition, several other studies[26,36] examined the effect of detergents and dispersants on the decomposition reactions and the synergy between the different oil additives. Some of these XAS measurements were combined with X-ray photoelectron emission microscopy (X-PEEM)[27,31,37] and photoelectron emission microscope by synchrotron undulator illumination technique.[38] A review of the different contributions of these various XAS techniques to tribology was provided by Nicholls *et al.*,[27] which highlighted the importance of XAS especially in studying the reactions of oil additives and the composition of the formed tribofilms.

Although the majority of the previous studies focused on using mainly *ex situ* techniques, there are also a number of studies that attempted to probe the chemistry and composition of various materials using *in situ* techniques such as vacuum XPS,[39,40] Raman spectroscopy,[23,41] and Attenuated Total Reflectance (ATR)-FTIR.[42,43] However, these techniques have some drawbacks in addition to their advantages. For instance, despite the surface sensitivity of the UHV-XPS technique, the need for a high vacuum environment necessitates that the tribological experiments to be performed in dry condition without the use of liquid lubricants and additives. The use of Raman spectroscopy can overcome this problem as the surface analysis can be performed under ambient atmosphere. However, not all the vibrational modes of the tribofilm constituents are expected to be Raman active, which depends on the spectroscopic selection rules that require a change in the polarizability of the molecule.[44] Furthermore, this technique has a large sampling depth, which makes it surface insensitive.[45] In addition, the need to use a transparent sapphire window as one of the counterparts adds a fingerprint of this material to the acquired data. The sapphire window also limits the usage of this technique to an inert surface which slides past another surface. The ATR-FTIR technique solves this problem by utilizing the total internal reflection through a germanium crystal that can be coated with a thin iron layer of few nanometers. Nevertheless, there are certain difficulties associated with this technique. Due to the ultra-thin coated layer on the crystal, the tribological tests cannot be performed under severe conditions involving wear, which limits the technique to mild operating conditions. Another issue with this technique is related to the possible change in the acquired signal depending on the following:[46] (i) the refraction index of the germanium crystal, which can change with temperature, (ii) any local variations in the thickness of the Fe coating on the germanium crystal, and (iii) the heterogeneity of the tribofilm thickness and composition, which can lead to variations in the penetration depth of the evanescent wave and effectively the sampling depth. These variations can affect both the intensity and chemical shift of the acquired signal.

In addition to these *in situ* techniques, there were numerous studies that utilized *in situ* XAS to study the evolution over time of different materials such as catalysts,[47,48] electrodes (cathode materials) of metal oxides,[49,50] and tribofilms of oil additives.[51,52] Morina *et al.*[51] and Ferrari *et al.*[52] studied the evolution of ZDDP thermal films *in situ* after different heating times using a heating cell combined with XAS. In order to have a surface sensitive signal, they performed the *in situ* experiments in the total external reflectance mode by tilting the samples to an angle less than the glancing angle. Nevertheless, so far, to our best knowledge, there are no reports on the *in situ* evolution of the tribofilms of oil additives under realistic conditions involving shear between contacting surfaces using the XAS technique. This study aims at developing a technique that allows examining the composition of these tribofilms *in situ* under the same testing conditions after different shearing times. This should provide a better understanding of the additives decomposition reactions and their kinetics without altering the sample condition. As a case study, this newly developed techniques will be used to follow the composition of ZDDP additives after different shearing times while keeping the sample at the same testing conditions, i.e., the same temperature and without rinsing the surface or altering its state.

II. TRIBOTESTER DESIGN

The designed tribotester shown in Fig. 1 is considered a pin-on-disc apparatus in which the disc is rotating and the pin is stationary. The rotation of the disc is achieved using an Electronically Commutated (EC) flat brushless motor (Maxon Motor, Switzerland) of 12 pole pairs. The motor has a nominal torque of 0.444 Nm, which is larger than the calculated needed torque of 0.25 Nm at 50 N maximum load and thus there was no need to use a gearbox. The motor has a diameter of 90 mm and a velocity range of 30–3000 rpm, or 0.15–15 m/s calculated at the central diameter of a wear scar of 97.5 mm. The detection of the rotor position was performed using three digital hall sensors whereas the speed control

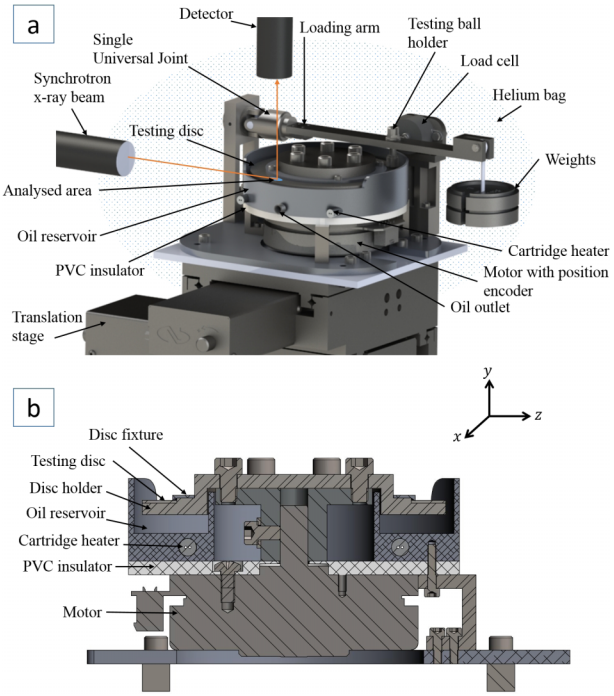

FIG. 1. Schematic of (a) the assembly and (b) a cross section of the tribological apparatus used in the *in situ* XAS experiments. The synchrotron X-ray incident beam and the XRF and XAS detectors are also shown in (a). The detector is placed in the vertical geometry at a right angle relative to both the incident beam and the tribological surface.

was performed in a closed loop mode using a MILE digital incremental encoder (Maxon Motor, Switzerland), which has a resolution of 6400 counts/turn. The speed resolution at zero load condition was better than ±0.1 rpm (0.5 mm/s) whereas at 50 N it was better than ±2 rpm (10 mm/s), which was verified by monitoring the real speed of the motor read by the encoder at 30, 50, and 100 rpm.

The disc has a standard dimension of 1 mm thickness, 110 mm outer diameter, and 85 mm inner diameter. The large size was chosen in order to increase the curvature of the wear scar and thus make it easier to be identified. In addition, the large size allows a larger area of the wear scar to be scanned during the XAS experiments and thus obtaining a more accurate averaged signal. The disc was fitted on a lower extruded surface of 1.9 mm depth and 85 mm diameter on the disc holder. To secure the disc, a fixture of a washer shape with a 1 mm protrusion at its outer diameter was screwed to the disc holder and tightened on the disc. The disc holder itself was closely fitted to the motor shaft in order to maximize the power transfer efficiency and reduce the backlash.

The pin of the apparatus consists of a ball fixed at one face without any allowed rotation using an M5 socket head cap screw. The standard size of the ball that was used during the XAS experiments was 5.5 mm, although smaller and larger sizes, i.e., 5, 6, and 6.5 mm, can be permitted as well.

The oil reservoir containing the disc and its holder was heated using two 300 W FIREROD cartridge heaters (Watlow Electric Manufacturing Co., USA) of 1/4″ diameter and 4″ length. These heaters were controlled in a closed-loop mode using an EZ-ZONE controller of two integrated PID channels (Watlow Electric Manufacturing Co., USA). The temperature of the oil was measured using two K-type thermocouples embedded in the middle location of the cartridge heaters. Using two thermocouples instead of one insures the homogeneity of temperature throughout the oil reservoir by controlling the temperature at two different locations.

The load was applied using calibrated slotted test weights on a hanger attached to the end of a loading arm. The alignment of this arm and the apparatus was checked using an electronic spirit level (Magnetic DXL360S Digital Protractor angle finder, 360° inclinometer), which has a resolution of 0.01°, accuracy of 0.05°, and measuring range of 360° for a single axis and ±40° for dual axis.

The friction force was measured using a compression load cell (Phidgets, Inc., Canada). The cell has a load capacity ranging from 0 to 4.5 kg. Figure 2 shows the friction force calibration curve for the friction load cell of the tribotester. In the range of the measured force, the output voltage increases linearly with the added weights with a slope of 0.9 V/kg, which is slightly different from the one of 1.0 V/kg suggested by the manufacturer. The creep of the load cell was found to be ±0.5 mV/h, which is within the long term deviation creep of 5 mV, i.e., about 50 g, suggested by the manufacturer.

III. EXPERIMENTAL METHODS

A. Materials and operating conditions

The oil used in this study was a poly-α-olefin oil, which contains zinc dialkyldithiophosphate antiwear additive (P concentration: 0.08%). The viscosity of the oil at 100 °C is 4.2 cSt and at 40 °C is 18.7 cSt, which corresponds to a viscosity index of 131. The counterbodies consisted of a ball, which is fixed and free of rolling, and a disc, which rotates with the motor. The disc has a diameter of 110 mm and was made of spring steel (AISI 1074 / SAE 5165) of average hardness of 47 on the Rockwell scale. The ball has a diameter

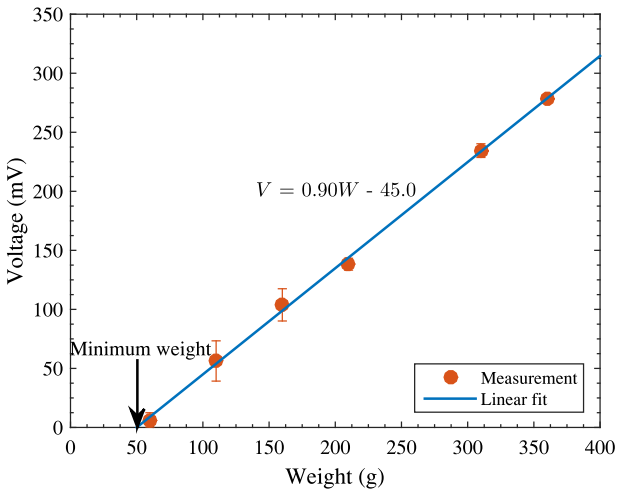

FIG. 2. Friction force calibration curve of the compression load cell used in the tribotester. The calibration equation used to fit the experimental data and the minimum weight detectable by the load cell are indicated.

TABLE I. List of the experimental conditions during the *in situ* XAS measurements.

Parameter	Value
Temperature (°C)	80
Load (Kg)	1.9
Contact pressure (GPa)	2.2
Sliding speed (rpm)	50
Shearing time (min)	2.5, 5, 10, 20, 30, and 60

of 5.5 mm and was made of grade 100 hardened steel (AISI 52100) of average hardness of 64 on the Rockwell scale.

The experimental conditions during the *in situ* XAS experiments are summarized in Table I. The large contact pressure, low sliding speed, and low hardness of the disc compared to the ball indicate that a clear wear scar should appear on the disc, as the experiments were performed in the boundary lubrication regime in which asperity-asperity contact occurs. This was verified by the visual inspection of the disc even after a few seconds of shearing.

The experiments were performed under a helium environment. The choice of helium is advantageous in many ways. The low atomic number helium reduces absorption of low-energy phosphorus and sulfur fluorescence signals. In addition, owing to its unique characteristics of being colorless, odorless, non-toxic, and non-flammable gas it can be used at ambient and high temperatures without health risks. Furthermore, helium is an inert gas and thus it is not expected to interact or react with the metal surface or the oil and its additives. The helium environment also helps exclude water contamination, which originates from the humidity carried by the ambient air, from affecting the chemical reactions under study. Although this is different from the real testing conditions that are affected by the presence of oxygen and water, it helps understanding the fundamental reactions with less complexity by excluding these factors. The principal theory regarding the decomposition mechanisms of ZDDP suggests that they can be thermal,[53,54] thermo-oxidative,[13,55] hydrolytic,[54] or hybrid. Focusing our attention on one mechanism only, i.e., thermal, helps understanding the extent of contribution of the other mechanisms by comparing our results with the ones reported in the literature under more realistic conditions.

During the acquisition of the XAS spectra, shearing was stopped but the temperature control was maintained. Although for real *in situ* experiments the test conditions should not be altered, stopping shearing during the spectra acquisition was performed in order to obtain time-resolved information both inside and outside the wear scar. This is the first step towards a complete *in situ* technique by acquiring the signal while the disc is rotating, which is planned for the next beam time.

The location of the wear scar on the disc was identified by elemental mapping of P and S using scanning micro-X-ray fluorescence (XRF) mapping, as shown in Fig. 3 plotted using PyMca application (version 5.1.1). The maps were acquired from an area of 1.75 mm × 0.40 mm by moving the tribotester in the lateral direction (x), in the horizontal plane perpendicular to the incident beam, from −0.40 mm to 1.35 mm with a step size of 0.01 mm and changing its height along the y-axis, in the vertical plane, from −0.80 mm to −1.20 mm with a step size of 0.02 mm. The mapping was performed using an excitation energy of 2600 eV, which is sufficient to observe the K shell peaks for both P and S elements of interest as it is about 3000 eV higher than the maximum $k\alpha$ emission energy of P (2010 eV) and S (2309 eV). The energy window for the $k\alpha$ P peak was defined between 1880 eV and 2100 eV whereas for the $k\alpha$ S peaks was defined between 2200 eV and 2400 eV. During acquisition, the data were analyzed online through the GDA (Generic Data Acquisition) software (version 8.34) associated with beam I18 by fitting the spectra with Gaussian peaks at the regions of interest and subtracting the background using a linear fit. The regions considered inside and outside the wear scar as specified in Fig. 3 were determined based on the diameter of the wear scar and footprint of the beam. As the rig is designed such that the ball shears the disc in the middle region between its internal and external diameters, this results in a wear scar diameter of 97.5 mm measured from the center of the disc. Taking into account that the rig was at a glancing angle of 2°, and the width and length of the incident beam were 50 μm and 200 μm, respectively, this produced a beam footprint of 50 μm × 2800 μm on the disc. Due to the large diameter of the wear scar, the region inside the wear scar can accommodate a beam footprint up

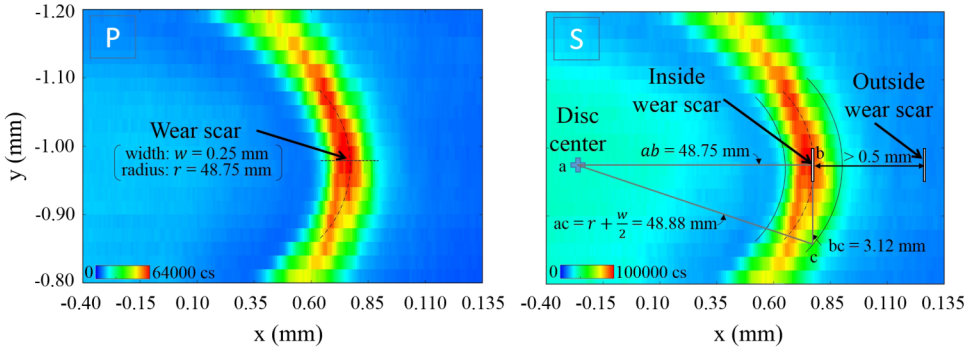

FIG. 3. XRF maps (1.75 × 0.40 mm^2) of the distributions of P (left) and S (right) elements found on the disc after 10 min of shearing time. The maps were captured by scanning the disc surface in the lateral direction along lines of 1.75 mm and in the vertical direction at different heights of 0.4 mm relative to the incident beam. The schematic of the right-angled triangle abc (not to scale) was used to identify the size of the areas considered inside and outside the wear scar.

to 6.2 mm. To insure that the signal is within the wear scar without overlapping with regions from outside, the beam was centered in the middle point of the wear scar at the brightest and furthest spot to the left of the disc, as shown in Fig. 3. The region outside the wear scar was selected to be at the same y-coordinate of the region inside the wear scar, i.e., the same sample height, but with an x-coordinate greater than 0.5 mm.

After the XFR maps acquisition and sample positioning, the XAS spectra of P and S k-edges were acquired in two locations. That is, one inside and one outside the wear scar, which took typically about 15 min/scan. The scans were repeated 3 times to obtain a better signal to noise ratio, although a good ratio was also obtained using a single scan only. The scanning parameters of the pre-edge, edge and post-edge regions of S and P k-edges were as follows. The pre-edge energy step was fixed at 3 eV with a time step of 0.5 s. The edge energy step was fixed at 1 eV with a time step of 0.5 s. Finally, the EXAFS step was set to a high resolution of 0.1 eV with a long time step of 3 s in order to obtain a better signal for data fitting and analysis. Finally, Athena software (version 0.9.24) was used to correct the background and normalize the acquired data following standard procedures suggested by Ravel and Newville.[56]

B. Beamline and detector setup

The XAS experiments were performed using the I18 microfocus spectroscopy beamline at the Diamond Light Source-Oxford (UK). The technical details of this beamline were discussed in detail by Mosselmans *et al.*[57] The I18 has an X-ray beam of a high spatial resolution of 2 μm × 2 μm and energy range between 2.05 keV and 20.5 keV. The high spatial resolution of this beamline allows the analysis of heterogeneous samples such as ZDDP tribofilms by providing insight into the local variations in composition. The P and S k-edges were acquired using the fluorescence yield (FY) mode. The fluorescence detector (Hitachi, USA), which was positioned vertically at a distance 20 cm above the sample, was a four-element Vortex-Maine 4 silicon drift detector with Xspress3 electronics processing (Quantum Detectors, UK). It should be noted that the vertical geometry of the detector relative to the surface can have a detrimental effect on the acquired signal especially for thick and concentrated samples. It can increase the elastic and Compton scattering by at least one order of magnitude, which can result in an overall decrease in the signal to noise ratio and deterioration of the peaks heights.[58] However, although the vertical geometry worsens the inevitable attenuation of the signal amplitude, it has a negligible effect on the energy shifts. Thus, for comparing the positions of different peaks under the same conditions, the vertical measurement geometry is sufficient.

As in the FY mode, X-ray beam can easily penetrate the formed tribofilm, which has a few tens of nanometers thickness, the technique is mostly considered surface insensitive. However, the surface sensitivity can be largely increased by aligning the sample below the critical glancing angle relative to the incident beam. This results in a total external reflection with an evanescent wave interacting with only a few nanometers, i.e., less than 10 nm, of the surface layers and decaying exponentially with the penetration depth. The critical angle θ_c can be given by[59]

$$\theta_c = \sqrt{\frac{N_A \rho r_e \lambda^2 f_1^0(\lambda)}{A\pi}}, \tag{1}$$

where N_A is Avogadro's number (6.022×10^{23} atoms/mol), ρ is the density (g/cm^3), A is the atomic mass (g/mol) of the probed element, r_e is the classical electron radius (2.818×10^{-13} cm), λ is the wavelength (cm) of the incident beam, and $f_1^0(\lambda)$ is the real part of the complex atomic scattering factor, which for primary X-rays can be approximated to the first order by the atomic number Z of the target. Using a simplistic assumption that the tribofilm consists mainly of sulfur ($\rho = 2.1$ g/cm^3) or phosphorous ($\rho = 1.8$ g/cm^3), Equation (1) suggests that the average critical glancing angle is less than 0.73°, as shown in Fig. 4, for both P and S at their average k-edge of 2150 eV and 2473 eV, respectively. A more realistic assumption that the ZDDP tribofilm consists mainly of zinc polyphosphate[7] ($\rho = 3.3$ g/cm^3 [60]) suggests a critical glancing angle of 0.80°.

Another parameter that is as important as the glancing angle is the penetration depth of the incident beam into the probed sample. The probed penetration depth z at any angle α_1 around the critical glancing angle is given by[59]

$$z = \frac{\lambda}{4\sqrt{2}\pi} \frac{1}{\left[\sqrt{\left(\alpha_1^2 - \theta_c^2\right)^2 + 4\beta^2} - \left[\alpha_1^2 - \theta_c^2\right]\right]^{1/2}}, \tag{2}$$

where β is the imaginary part of the refractive index, which is related to the mass attenuation coefficient, μ/ρ (g/cm^4) reported for different materials,[61] as follows:

$$\beta = \frac{\lambda}{4\pi}\left(\frac{\mu}{\rho}\right)\rho, \tag{3}$$

where μ is the linear attenuation coefficient (cm^{-1}) and ρ is the density of the probed element (g/cm^3). A simpler formula for the penetration depth z at an angle much less than this

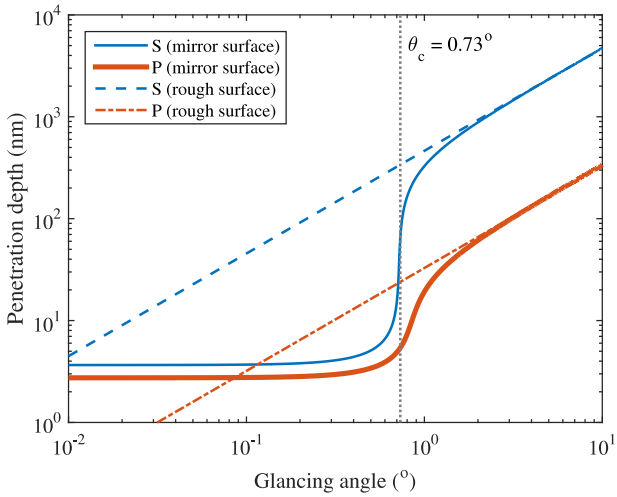

FIG. 4. Penetration depth as a function of the glancing angle for smooth and rough surfaces calculated at the k-edge of S and P. The vertical dotted line marks the average critical angle for total external reflection for both P and S.

critical angle, e.g., 0.1°, can be given by

$$z = \frac{\lambda}{4\pi\theta_c}. \quad (4)$$

Figure 4 shows the change in the penetration depth with the glancing angle calculated for P and S at their k-edge photon energy. For an angle much below the critical angle, it is possible to achieve a surface sensitivity of approximately 3 nm for both S and P. However, this is only true in the case of a mirror smooth surface at which the specular reflection can result in a total external reflection. On the other hand, for rough surfaces, diffuse reflection causes the loss of the total external reflection and therefore the penetration depth becomes a linear function of the glancing angle.

As the disc surface has a 0.1 μm root-mean square (RMS) roughness and similarly the patchy tribofilm formed on the surface, this condition does not favor the total external reflection. Therefore, the disc was held at an incident angle of 2° relative to the incident beam, which should give penetration depths greater than 100 nm and 1 μm for P and S, respectively. This should allow us to probe the whole thickness of the tribofilm and track its overall compositional changes as a function of time instead of the top surface layers only.

IV. RESULTS AND DISCUSSION

A. Characterization of P *k*-edge

Figures 5 and 6 show the evolution of the normalized P k-edge spectra outside and inside the wear scar after different shearing times. The ability to observe and distinguish different features in the P signal during the tribological test demonstrates the feasibility of this *in situ* technique to unravel more information than what is possible using *ex situ* techniques. Furthermore, the clear and strong peaks indicate that the detrimental scattering effect due to the vertical geometry of the detector, which was discussed in Section III B is minimum.

The P k-edge spectra appeared to have four main peaks. The first one, peak (a), appears at the low energy range at 2150.4 eV, which corresponds to unreacted ZDDP adsorbed to the steel surface. The second peak (b) appears at 2152.2 eV, which can be assigned to zinc phosphate whether of short or long phosphate chains.[34,36,51] The absence of a distinctive pre-edge peak at 2148.0 eV indicates that the iron (III) phosphate ($FePO_4$) of short chains is absent or of low concentration but does not provide any information regarding the presence of any iron phosphates of longer chains.[32] Additional two peaks, (c) and (d), appear at 2160.0 eV and 2169.0 eV, respectively, in the high energy post-edge region. The presence or absence of these two peaks can be related to the structure and composition of the formed phosphate. The post-edge peaks can provide information regarding the oxidation state and arrangements of the different elements within the phosphate glass structure composing the tribofilm.[62]

The P k-edge spectra show different subtle changes whether inside or outside the wear scar, which can provide insight into the composition of the formed tribofilm. The main changes are related to the evolution of peak (a) relative to peak (b) and the presence of the post-edge peaks over shearing time.

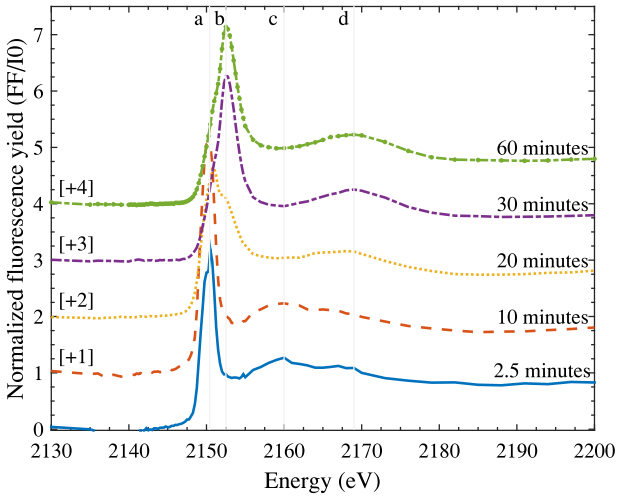

FIG. 5. Evolution of the normalized fluorescence yield (FF/I0) spectra of P k-edge outside the wear scar after different shearing times showing the transient changes in two main peaks, i.e., a: unreacted ZDDP at 2150.4 eV and b: zinc phosphate at 2152.2 eV, and two high energy peaks, i.e., c: at 2160.0 eV and d: at 2169.0 eV. Each curve is vertically offset for clarity by adding a constant, as specified on each curve, relative to the first curve.

Outside the wear scar, during the initial stage of the test, i.e., after 2.5 min, the low energy peak (a) corresponding to unreacted ZDDP dominates the higher energy peak (b) corresponding to zinc phosphate. As heating continued, ZDDP is consumed to form phosphate glass, which is obvious from the substantial decrease in the height of peak (a) of the unreacted ZDDP along with the simultaneous increase in the height of peak (b) of zinc phosphate. After 30 min, the individual peak (a) becomes convoluted in peak (b) and appears as a shoulder. Similar conclusions can also be drawn from the height and photon energy of the post-edge peaks (c)

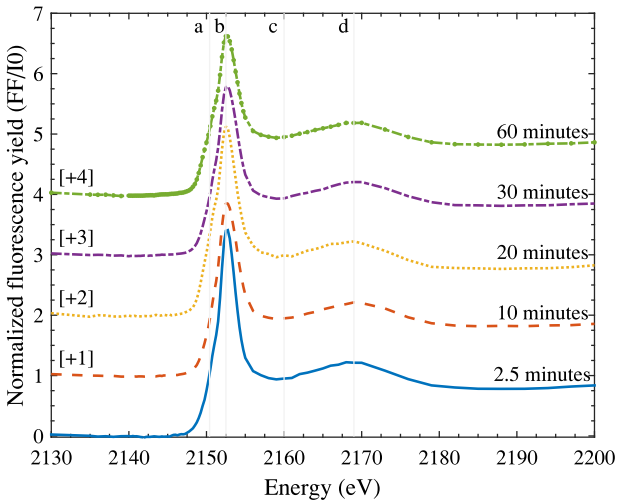

FIG. 6. Evolution of the normalized fluorescence yield (FF/I0) spectra of P k-edge inside the wear scar after different shearing times showing the transient changes in two main peaks, i.e., a: unreacted ZDDP at 2150.4 eV and b: zinc phosphate at 2152.2 eV, and two high energy peaks, i.e., c: at 2160.0 eV and d: at 2169.0 eV. Each curve is vertically offset for clarity by adding a constant, as specified on each curve, relative to the first curve.

and (d). At short heating times, these peaks are present as distinctive peaks. As heating continued, the height of peak (c) decreases until it disappears after 10 min whereas the height of peak (d) shows an opposite trend. This progressive change with heating time suggests a change in the composition of the thermal film matrix and the length of the formed phosphate chains.

The evolution of the P *k*-edge spectra inside the wear scar shows inconspicuous common changes over time as compared to the ones outside the wear scar. For instance, from the beginning peak (a) appears to be convoluted in peak (b) and exists as a shoulder, as compared to the case outside the wear scar when this starts to occur after 30 min. In addition, peak (c) is absent and only peak (d) appears in the post-edge region. The main reason behind this invariant trend can be explained as follows. As these experiments were not carried out at the critical glancing angle, the acquired XAS signal originates from not only the surface layer but also the bulk layers. Therefore, the common features of the spectra over shearing time indicate that the average composition of the tribofilm is unchanged. This can be mainly related to the nature of the ZDDP decomposition outside the wear, which is only thermally activated, as compared to the one inside the wear scar, which is thermally activated and mechanically assisted process.[15] This indicates that the ZDDP decomposition inside the wear scar will be faster as the decomposition is assisted by shear. The steady-state composition of the tribofilm can be reached as early as after 2.5 min whereas the slow evolution of the thermal film takes a longer period. This becomes evident by noticing that only after 30 min does the spectrum of the thermal film start to match the initial spectrum of the tribofilm after 2.5 min of shear.

B. Characterization of S *k*-edge

The evolution of the normalized S *k*-edge spectra outside and inside the wear scar after different shearing times is shown in Figs. 7 and 8, respectively. The clear change observed after the different heating and shearing times confirm the advantage of using this *in situ* technique for following the chemical changes without interfering with the sample or the testing conditions. The S *k*-edge spectra appeared to have three main and three secondary peaks. The first main peak, (a), appears in the pre-edge region at 2469.5 eV, which can be related to the presence of FeS.[36] The second main peak, (b), appears at 2473.0 eV, which can be assigned to ZnS or alkyl sulfide.[31] The third main peak, (c), appears at 2481.9 eV, which can be attributed to $ZnSO_4$[36] or FeSO4.[33,36]

The three other secondary peaks appear especially at short shearing or heating times. The first two, peak (d) and (e), which appear at 2475.5 eV and 2477.0 eV, respectively, can be related to alkyl disulfide from the adsorbed ZDDP.[36] On the other hand, the third secondary peak, (f), which appears at 2499.0 eV, can be mainly related to the presence of sulfate species.

The evolution of S *k*-edge inside and outside the wear scar showed similar trends. Initially, after heating or shearing for a short period of time, e.g., 2.5 min, the sulfur composing

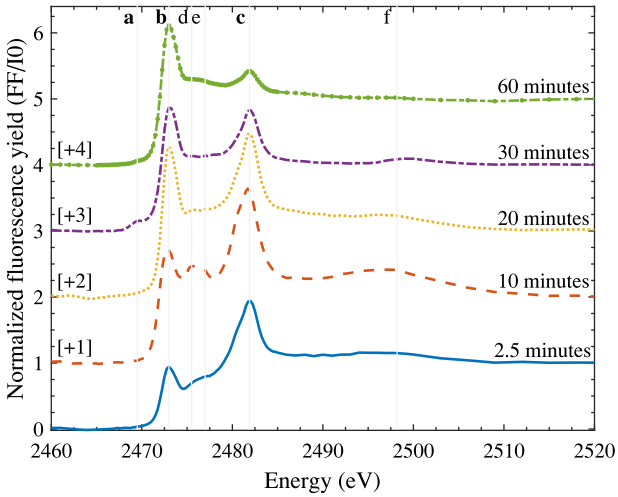

FIG. 7. Evolution of the normalized fluorescence yield (FF/I0) spectra of S *k*-edge outside the wear scar after different shearing times showing the change in three main peaks, i.e., a: FeS at 2469.5 eV, b: ZnS or alkyl sulfide at 2473.0 eV, and c: $ZnSO_4$ or $FeSO_4$ at 2481.9 eV, and three secondary peaks, i.e., d: alkyl disulfide at 2475.5 eV, e: alkyl disulfide at 2477.0 eV, and f: sulfate species at 2499.0 eV. Each curve is vertically offset for clarity by adding a constant, as specified on each curve, relative to the first curve.

the tribofilm appears mainly in the oxidized form of sulfate with only a small concentration of the reduced sulfide form. However, after longer shearing or heating times, the sulfate concentration decreases whereas the sulfide concentration increases, as indicated in the change of heights of peak (b) and (c). These observations are in agreement with the previously reported *ex situ* XAS study of Yin *et al.*,[55] which found that sulfate can form in the tribofilm during the early stage of the test. This was related to the high temperature at the contacting asperities during the running-in period due to surface smearing and wear, which favors the formation of sulfate. However, after smoothing the rough asperities the

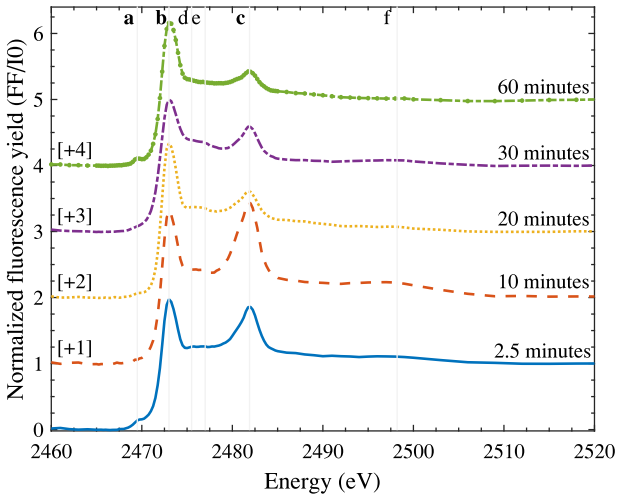

FIG. 8. Evolution of the normalized fluorescence yield (FF/I0) spectra of S *k*-edge inside the wear scar after different shearing times showing the change in three main peaks, i.e., a: FeS at 2469.5 eV, b: ZnS or alkyl sulfide at 2473.0 eV, and c: $ZnSO_4$ or $FeSO_4$ at 2481.9 eV, and three secondary peaks, i.e., d: alkyl disulfide at 2475.5 eV, e: alkyl disulfide at 2477.0 eV, and f: sulfate species at 2499.0 eV. Each curve is vertically offset for clarity by adding a constant, as specified on each curve, relative to the first curve.

local temperature at the asperity contacts drops below the critical temperature for sulfate formation and thus the more stable ZnS is expected to form instead.

V. CONCLUSION

We have designed a mini pin-on-disc tribotester that can be coupled with XAS to perform *in situ* tribological tests at different loads, temperatures, and sliding speeds. Using this apparatus, it was possible to follow and examine the evolution of the ZDDP tribofilm composition over time through the measurements of the *k*-edge XAS spectra of P and S. The unique feature of this apparatus is that, for the first time, the composition of ZDDP tribofilms and thermal films can be studied at ambient pressure without altering the sample condition.

The *in situ* XAS results suggested that the concentration of zinc phosphate in the ZDDP thermal film outside the wear scar increases progressively until it reaches the concentration of the zinc phosphate in the tribofilm inside the wear scar. This confirms the findings of previous studies that suggested that the decomposition of ZDDP is a thermally activated mechanically assisted process. The results also showed that at the beginning of the test, ZDDP tribofilms and thermal films consist of sulfur mainly in the form of sulfate with some disulfide, which progressively changes into sulfide.

The findings of this study widens the scope of the future investigations to study the reaction kinetics of different materials under shear and realistic test conditions. It also opens opportunities to study the evolution over time of ZDDP additive on different surfaces and its interaction with other oil additives under heat and shear.

ACKNOWLEDGMENTS

The authors would like to express their grateful acknowledgment to the financial support of Marie Curie Initial Training Networks (ITN) - FUTURE-BET project, Grant No. 317334. We also thank Diamond Light Source for access to beamline I18 (Proposal No. SP12907) that contributed to the results presented here.

[1]K. Holmberg, P. Andersson, and A. Erdemir, "Global energy consumption due to friction in passenger cars," Tribol. Int. **47**, 221–234 (2012).
[2]U. D. Schwarz, "Tracking antiwear film formation," Science **348**(6230), 40–41 (2015).
[3]B. Bhushan, *Micro/Nanotribology and Its Applications*, Nato Science Series E (Springer, Netherlands, 2012).
[4]P. Jost, Lubrication (Tribology) – A Report On The Present Position And Industry's Needs, 1966.
[5]S.-w. Zhang, "Green tribology: Fundamentals and future development," Friction **1**(2), 186–194 (2013).
[6]T. Onodera, Y. Morita, A. Suzuki, M. Koyama, H. Tsuboi, N. Hatakeyama, A. Endou, H. Takaba, M. Kubo, F. Dassenoy *et al.*, "A computational chemistry study on friction of h – MoS_2. Part I. Mechanism of single sheet lubrication," J. Phys. Chem. B **113**(52), 16526–16536 (2009).
[7]H. Spikes, "The history and mechanisms of ZDDP," Tribol. Lett. **17**(3), 469–489 (2004).
[8]J. C. Bell, K. M. Delargy, and A. M. Seeney, "Paper IX (ii) The removal of substrate material through thick zinc dithiophosphate anti-wear films," Tribol. Ser. **21**, 387–396 (1992).
[9]P. A. Willermet, D. P. Dailey, R. O. Carter, P. J. Schmitz, and W. Zhu, "Mechanism of formation of antiwear films from zinc dialkyldithiophosphates," Tribol. Int. **28**(3), 177–187 (1995).
[10]S. Bec, A. Tonck, J.-M. Georges, and G. W. Roper, "Synergistic effects of MoDTC and ZDTP on frictional behaviour of tribofilms at the nanometer scale," Tribol. Lett. **17**(4), 797–809 (2004).
[11]J. M. Martin, C. Grossiord, T. Le Mogne, S. Bec, and A. Tonck, "The two-layer structure of Zndtp tribofilms: Part I: AES, XPS and XANES analyses," Tribol. Int. **34**(8), 523–530 (2001).
[12]J. M. Martin, "Antiwear mechanisms of zinc dithiophosphate: A chemical hardness approach," Tribol. Lett. **6**(1), 1–8 (1999).
[13]M. L. S. Fuller, M. Kasrai, G. M. Bancroft, K. Fyfe, and K. H. Tan, "Solution decomposition of zinc dialkyl dithiophosphate and its effect on antiwear and thermal film formation studied by X-ray absorption spectroscopy," Tribol. Int. **31**(10), 627–644 (1998).
[14]M. A. Nicholls, P. R. Norton, G. M. Bancroft, M. Kasrai, G. De Stasio, and L. M. Wiese, "Spatially resolved nanoscale chemical and mechanical characterization of ZDDP antiwear films on aluminum–silicon alloys under cylinder/bore wear conditions," Tribol. Lett. **18**(3), 261–278 (2005).
[15]N. N. Gosvami, J. A. Bares, F. Mangolini, A. R. Konicek, D. G. Yablon, and R. W. Carpick, "Mechanisms of antiwear tribofilm growth revealed *in situ* by single-asperity sliding contacts," Science **348**(6230), 102–106 (2015).
[16]S. Equey, S. Roos, U. Mueller, R. Hauert, N. D. Spencer, and R. Crockett, "Reactions of zinc-free anti-wear additives in DLC/DLC and steel/steel contacts," Tribol. Int. **41**(11), 1090–1096 (2008).
[17]B. Vengudusamy, J. H. Green, G. D. Lamb, and H. A. Spikes, "Tribological properties of tribofilms formed from ZDDP in DLC/DLC and DLC/steel contacts," Tribol. Int. **44**(2), 165–174 (2011).
[18]H. Cen, A. Morina, A. Neville, R. Pasaribu, and I. Nedelcu, "Effect of water on ZDDP anti-wear performance and related tribochemistry in lubricated steel/steel pure sliding contacts," Tribol. Int. **56**, 47–57 (2012).
[19]P. A. Willermet, D. P. Dailey, R. O. Carter III, P. J. Schmitz, W. Zhu, J. C. Bell, and D. Park, "The composition of lubricant-derived surface layers formed in a lubricated cam/tappet contact II. Effects of adding overbased detergent and dispersant to a simple ZDTP solution," Tribol. Int. **28**(3), 163–175 (1995).
[20]G. C. Smith, "Evaluation of a simple correction for the hydrocarbon contamination layer in quantitative surface analysis by XPS," J. Electron Spectrosc. Relat. Phenom. **148**(1), 21–28 (2005).
[21]S. Bec, A. Tonck, J.-M. Georges, R. C. Coy, J. C. Bell, and G. W. Roper, "Relationship between mechanical properties and structures of zinc dithiophosphate anti–wear films," Proc. R. Soc. A **455**, 4181–4203 (1999).
[22]J. Ye, S. Araki, M. Kano, and Y. Yasuda, "Nanometer-scale mechanical/structural properties of molybdenum dithiocarbamate and zinc dialkylsithiophosphate tribofilms and friction reduction mechanism," Jpn. J. Appl. Phys., Part 1 **44**(7S), 5358 (2005).
[23]S. Berkani, F. Dassenoy, C. Minfray, M. Belin, B. Vacher, J. M. Martin, H. Cardon, G. Montagnac, and B. Reynard, "Model formation of ZDDP tribofilm from a mixture of zinc metaphosphate and goethite," Tribol. Int. **79**, 197–203 (2014).
[24]S. Berkani, F. Dassenoy, C. Minfray, J.-M. Martin, H. Cardon, G. Montagnac, and B. Reynard, "Structural changes in tribo-stressed zinc polyphosphates," Tribol. Lett. **51**(3), 489–498 (2013).
[25]M. Aktary, M. T. McDermott, and J. Torkelson, "Morphological evolution of films formed from thermooxidative decomposition of ZDDP," Wear **247**(2), 172–179 (2001).
[26]M. A. Nicholls, G. M. Bancroft, P. R. Norton, M. Kasrai, G. De Stasio, B. H. Frazer, and L. M. Wiese, "Chemomechanical properties of antiwear films using X-ray absorption microscopy and nanoindentation techniques," Tribol. Lett. **17**(2), 245–259 (2004).
[27]M. Nicholls, M. N. Najman, Z. Zhang, M. Kasrai, P. R. Norton, and P. U. P. A. Gilbert, "The contribution of XANES spectroscopy to tribology," Can. J. Chem. **85**(10), 816–830 (2007).
[28]Z. Zhang, E. S. Yamaguchi, M. Kasrai, and G. M. Bancroft, "Tribofilms generated from ZDDP and DDP on steel surfaces: Part 1, growth, wear and morphology," Tribol. Lett. **19**(3), 211–220 (2005).
[29]Y.-R. Li, G. Pereira, A. Lachenwitzer, M. Kasrai, and P. R. Norton, "Studies on ZDDP thermal film formation by XANES spectroscopy, atomic force microscopy, FIB/SEM and 31P NMR," Tribol. Lett. **29**(1), 11–22 (2008).
[30]M. N. Najman, M. Kasrai, G. M. Bancroft, B. H. Frazer, and G. De Stasio, "The correlation of microchemical properties to antiwear (AW) performance in ashless thiophosphate oil additives," Tribol. Lett. **17**(4), 811–822 (2004).
[31]K. Masenelli-Varlot, M. Kasrai, G. M. Bancroft, G. De Stasio, B. Gilbert, E. S. Yamaguchi, and P. R. Ryason, "Spatial distribution of the chemical

species generated under rubbing from ZDDP and dispersed potassium triborate," Tribol. Lett. **14**(3), 157–166 (2003).
[32]M. N. Najman, M. Kasrai, G. M. Bancroft, and A. Miller, "Study of the chemistry of films generated from phosphate ester additives on 52100 steel using X-ray absorption spectroscopy," Tribol. Lett. **13**(3), 209–218 (2002).
[33]M. N. Najman, M. Kasrai, and G. M. Bancroft, "X-ray absorption spectroscopy and atomic force microscopy of films generated from organosulfur extreme-pressure (EP) oil additives," Tribol. Lett. **14**(4), 225–235 (2003).
[34]M. A. Nicholls, T. Do, P. R. Norton, G. M. Bancroft, M. Kasrai, T. W. Capehart, Y.-T. Cheng, and T. Perry, "Chemical and mechanical properties of ZDDP antiwear films on steel and thermal spray coatings studied by XANES spectroscopy and nanoindentation techniques," Tribol. Lett. **15**(3), 241–248 (2003).
[35]M. Fuller, M. Kasraia, J. S. Sheasby, G. M. Bancroft, K. Fyfe, and K. H. Tan, "X-ray absorption spectroscopy of antiwear films on aluminum alloys generated from zinc dialkyldithiophosphate," Tribol. Lett. **1**(4), 367–378 (1995).
[36]Z. Zhang, M. Kasrai, G. M. Bancroft, and E. S. Yamaguchi, "Study of the interaction of ZDDP and dispersants using X-ray absorption near edge structure spectroscopy – Part 1: Thermal chemical reactions," Tribol. Lett. **15**(4), 377–384 (2003).
[37]M. A. Nicholls, P. R. Norton, G. M. Bancroft, M. Kasrai, T. Do, B. H. Frazer, and G. De Stasio, "Nanometer scale chemomechanical characterization of antiwear films," Tribol. Lett. **17**(2), 205–216 (2004).
[38]G. De Stasio, M. Capozi, G. F. Lorusso, P. A. Baudat, T. C. Droubay, P. Perfetti, G. Margaritondo, and B. P. Tonner, "MEPHISTO: Performance tests of a novel synchrotron imaging photoelectron spectromicroscope," Rev. Sci. Instrum. **69**(5), 2062–2066 (1998).
[39]C. Donnet, J. M. Martin, J. Fontaine, J. C. Sánchez-López, C. Quirós, E. Elizalde, J. M. Sanz, T. C. Rojas, and A. Fernández, "The role of CN chemical bonding on the tribological behaviour of CN_x coatings," Surf. Coat. Technol. **120**, 594–600 (1999).
[40]C. Donnet, J. Fontaine, A. Grill, and T. L. Mogne, "The role of hydrogen on the friction mechanism of diamond-like carbon films," Tribol. Lett. **9**(3-4), 137–142 (2001).
[41]M. Gauvin, F. Dassenoy, C. Minfray, J. M. Martin, G. Montagnac, and B. Reynard, "Zinc phosphate chain length study under high hydrostatic pressure by Raman spectroscopy," J. Appl. Phys. **101**(6), 063505 (2007).
[42]F. M. Piras, A. Rossi, and N. D. Spencer, "Combined *in situ* (ATR FT-IR) and *ex situ* (XPS) study of the ZnDTP-iron surface interaction," Tribol. Lett. **15**(3), 181–191 (2003).
[43]A. Rossi, M. Eglin, F. M. Piras, K. Matsumoto, and N. D. Spencer, "Surface analytical studies of surface-additive interactions, by means of *in situ* and combinatorial approaches," Wear **256**(6), 578–584 (2004).
[44]G. Socrates, *Infrared and Raman Characteristic Group Frequencies: Tables and Charts* (John Wiley & Sons, 2004).
[45]K. Kneipp, H. Kneipp, I. Itzkan, R. R. Dasari, and M. S. Feld, "Surface-enhanced Raman scattering and biophysics," J. Phys.: Condens. Matter **14**(18), R597 (2002).
[46]F. M. Piras, A. Rossi, and N. D. Spencer, "Growth of tribological films: *In situ* characterization based on attenuated total reflection infrared spectroscopy," Langmuir **18**(17), 6606–6613 (2002).
[47]T. L. Reitz, P. L. Lee, K. F. Czaplewski, J. C. Lang, K. E. Popp, and H. H. Kung, "Time-resolved XANES investigation of CuO/ZnO in the oxidative methanol reforming reaction," J. Catal. **199**(2), 193–201 (2001).
[48]M. M. Günter, T. Ressler, R. E. Jentoft, and B. Bems, "Redox behavior of copper oxide/zinc oxide catalysts in the steam reforming of methanol studied by *in situ* X-ray diffraction and absorption spectroscopy," J. Catal. **203**(1), 133–149 (2001).
[49]W.-S. Yoon, C. P. Grey, M. Balasubramanian, X.-Q. Yang, and J. McBreen, "In situ X-ray absorption spectroscopic study on $LiNi_{0.5}Mn_{0.5}O_2$ cathode material during electrochemical cycling," Chem. Mater. **15**(16), 3161–3169 (2003).
[50]Y. W. Tsai, B. J. Hwang, G. Ceder, H. S. Sheu, D. G. Liu, and J. F. Lee, "*In situ* X-ray absorption spectroscopic study on variation of electronic transitions and local structure of $LiNi_{1/3}Co_{1/3}Mn_{1/3}O_2$ cathode material during electrochemical cycling," Chem. Mater. **17**(12), 3191–3199 (2005).
[51]A. Morina, H. Zhao, and J. F. W. Mosselmans, "*In situ* reflection-XANES study of ZDDP and MoDTC lubricant films formed on steel and diamond like carbon (DLC) surfaces," Appl. Surf. Sci. **297**, 167–175 (2014).
[52]E. S. Ferrari, K. J. Roberts, M. Sansone, and D. Adams, "A multi-edge X-ray absorption spectroscopy study of the reactivity of zinc di-alkyl-dithiophosphates anti-wear additives: 2. *In situ* studies of steel/oil interfaces," Wear **236**(1), 259–275 (1999).
[53]F. T. Barcroft, R. J. Bird, J. F. Hutton, and D. Park, "The mechanism of action of zinc thiophosphates as extreme pressure agents," Wear **77**(3), 355–384 (1982).
[54]H. Spedding and R. C. Watkins, "The antiwear mechanism of zddp's. Part I," Tribol. Int. **15**(1), 9–12 (1982).
[55]Z. Yin, M. Kasrai, M. Fuller, G. M. Bancroft, K. Fyfe, and K. H. Tan, "Application of soft X-ray absorption spectroscopy in chemical characterization of antiwear films generated by ZDDP Part I: The effects of physical parameters," Wear **202**(2), 172–191 (1997).
[56]B. Ravel and M. Newville, "ATHENA and ARTEMIS: interactive graphical data analysis using IFEFFIT," Phys. Scr. **2005**(T115), 1007.
[57]J. F. W. Mosselmans, P. D. Quinn, A. J. Dent, S. A. Cavill, S. D. Moreno, A. Peach, P. J. Leicester, S. J. Keylock, S. R. Gregory, K. D. Atkinson *et al.*, "I18 – the microfocus spectroscopy beamline at the Diamond Light Source," J. Synchrotron Radiat. **16**(6), 818–824 (2009).
[58]G. Das, M. K. Tiwari, A. K. Singh, and H. Ghosh, "Effect of synchrotron polarization on grazing incidence X-ray fluorescence analysis," J. Anal. At. Spectrom. **29**(12), 2405–2413 (2014).
[59]R. Klockenkämper and A. von Bohlen, *Total-Reflection X-ray Fluorescence Analysis and Related Methods* (John Wiley & Sons, 2014).
[60]G. Walter, G. Goerigk, and C. Rüssel, "The structure of phosphate glass evidenced by small angle X-ray scattering," J. Non-Cryst. Solids **352**(38), 4051–4061 (2006).
[61]J. H. Hubbell and S. M. Seltzer, "Tables of X-ray mass attenuation coefficients and mass energy-absorption coefficients 1 kev to 20 MeV for elements Z = 1 to 92 and 48 additional substances of dosimetric interest," Technical Report NISTIR-5632, National Institute of Standards and Technology-PL, Gaithersburg, MD (United States), Ionizing Radiation Division 1995.
[62]E. D. Ingall, J. A. Brandes, J. M. Diaz, M. D. de Jonge, D. Paterson, I. McNulty, W. C. Elliott, and P. Northrup, "Phosphorus *k*-edge XANES spectroscopy of mineral standards," J. Synchrotron Radiat. **18**(2), 189–197 (2011).